Registration of phase contrast images in propagation-based X-ray phase tomography

Loriane Weber[1,2,*], Annika Hänsch[1,*], Uwe Wolfram[3], Alexandra Pacureanu[2], P. Cloetens[2], Françoise Peyrin[1,2], Simon Rit[1], Max Langer[1]

[*] Contributed equally

[1] Univ.Lyon, INSA-Lyon, Université Claude Bernard Lyon 1, CNRS UMR 5220, Inserm U1206, CREATIS, 69621 Lyon, France

[2] ESRF, The European Synchrotron Radiation, 38053 Grenoble, France

[3] Heriot-Watt University, School of Engineering and Physical Sciences (EPS), Institute of Mechanical, Process and Energy Engineering (IMPEE), EH14 4AS Edinburgh, UK

Abstract

X-ray phase tomography aims at reconstructing the 3D electron density distribution of an object. It offers enhanced sensitivity compared to attenuation-based X-ray absorption tomography. In propagation-based methods, phase contrast is achieved by letting the beam propagate after interaction with the object. The phase shift is then retrieved at each projection angle, and subsequently used in tomographic reconstruction to obtain the refractive index decrement distribution, which is proportional to the electron density. Accurate phase retrieval is achieved by combining images at different propagation distances. For reconstructions of good quality, the phase contrast images recorded at different distances need to be accurately aligned. In this work, we characterise the artefacts related to misalignment of the phase contrast images, and investigate the use of different registration algorithms for aligning in-line phase contrast images. This is done by a simulation study and comparison with experimental data. Loss in resolution due to vibrations is found to be comparable to attenuation-based computed tomography. Further, it is shown that registration of phase contrast images is non-trivial due to the difference in contrast between the different images, and the often periodical artefacts present in the phase contrast images if multi-layer X-ray optics are used. We found that using a mutual information based registration algorithm yielded more precise results on the simulated data, and was more robust than a correlation based method on experimental nano-tomography data.

Keywords phase tomography, registration, simulation, artefacts, nano-tomography, X-ray imaging

1 Introduction

X-ray phase contrast micro-computed tomography (μCT) is a relatively new imaging modality which offers several advantages for the investigation of biological samples, compared to standard attenuation μCT (Boistel et al., 2011; Zanette et al., 2011). Phase contrast μCT has been shown to be several orders of magnitude more sensitive than standard μCT (Momose & Fukuda, 1995), particularly in the hard X-ray domain. This is especially interesting for the imaging of structures in soft tissue (Guigay et al., 2007) (Horng et al., 2014). Further, due to the higher sensitivity, the dose absorbed by the sample can be kept lower than with attenuation based techniques. As opposed to attenuation, the phase of an X-ray beam cannot be measured directly, however. Several ways to achieve contrast derived from the phase of the X-ray beam have been invented (Zanette et al., 2013). In this work, we only consider free space propagation, known in the literature variously as Fresnel diffraction, in-line holography, and propagation based imaging (PBI).

PBI is implemented by letting a highly coherent and monochromatic X-ray beam propagate in free space after interaction with an object, before measuring with an X-ray imaging detector (Snigirev, et al. 1995). The resulting Fresnel diffraction patterns, or phase contrast images, can be used directly as input to a tomographic reconstruction algorithm, where it yields an edge enhancement effect. This is due to the phase contrast being sensitive approximately to the Laplacian of the phase of the wave-field. The resulting modality is called phase contrast tomography (Cloetens et al., 1997). While this can be an interesting modality in its own right, the non-linear quantitative relationship between phase shift and contrast can be used to reconstruct the phase shift. This inverse problem is called phase retrieval. Once the phase is retrieved, it can be used to reconstruct the 3D refractive index decrement distribution in the object. This imaging modality is called phase tomography (Cloetens et al., 1999; Herman, 2009; Langer et al., 2013). It has the advantage over phase contrast tomography of yielding a contrast that is proportional to the electron density (i.e. mass density for most materials) distribution, rather than edge contrast related to the second derivative of the refractive index decrement distribution.

Several algorithms for phase retrieval from Fresnel diffraction patterns have been developed. Most of these rely on linearisation of the Fresnel diffraction model to yield efficient algorithms using linear filtering (Cloetens et al., 1999; Guigay et al., 2007; Nugent et al, 1996). Two approaches commonly used for phase retrieval from Fresnel diffraction patterns are the Transport of Intensity Equation (TIE) (Nugent et al., 1996; Paganin et al. 2002; Teague, 1982) and the Contrast Transfer Function (CTF) (Cloetens et al., 1999; Guigay, 1977). The TIE is valid for short object-to-detector distances and the CTF is valid for objects with slowly varying phase and weak absorption.

Information transfer from phase shift to contrast in the low spatial frequency range is weak, which makes phase retrieval from Fresnel diffraction patterns sensitive to low frequency noise (Langer et al., 2010). Several approaches to overcome this limitation have been proposed. Paganin et al. (2002) introduced a homogeneity criterion on the object in the TIE, thus achieving a single distance phase retrieval algorithm. Object homogeneity has also been used in the CTF based methods, but rather introduced as an a priori on the low spatial frequencies of the phase (Langer et al., 2010). This approach has been extended to multi-material (Langer, Cloetens, et al., 2012) and heterogeneous objects (Langer et al., 2014) under the assumption that the sample composition is roughly known.

One particularity of the CTF-based methods is that they allow the use of several phase contrast images taken at different sample-to-detector distances. This allows for a better coverage of the recorded phase information in the frequency domain (Zabler et al., 2005), at the cost of increased acquisition time (notably camera displacement and extra reference images; the exposure time is not necessarily increased (Frachon et al., 2015)) and computational load (image registration of the phase contrast images taken at different distances). Using several distances seems necessary to achieve good image quality in high-resolution imaging (Langer, Pacureanu, et al., 2012). A similar problem exists in high resolution transmission electron microscopy, which is known as a through focal series reconstruction (Op de Beeck et al., 1996).

In these techniques however, the diffraction patterns at different distances need to be aligned. They can be out of alignment due to instrumental imprecisions, drift and vibrations. This problem has been mentioned only in passing in literature despite being non-trivial, especially at high resolution. Specifically, this is a registration problem where the images are similar but not identical, due to the different propagation distances. At lower resolution the contrast is reasonably similar in the images recorded at different distances, whereas at higher resolution the contrast can be very different at the different distances. Usually, this registration problem is handled using correlation based methods. In our experience, these approaches work well at relatively low resolutions and in the absence of strong artefacts (especially periodic artefacts such as stripes from X-ray multilayer monochromator optics), but fail more often as resolutions become higher. One reason may be that the intensity in the images can be quite different, whereas registration based on cross-correlation assumes that the intensities do not change, only the position of the image.

Therefore, the aim of this work is to investigate the impact of this registration step on the image quality in the final reconstructed phase tomography image. First, we conducted a simulation study to investigate qualitatively and quantitatively the impact of different misalignments resulting from different types of instrumental instability. We then compared the simulated artefacts to artefacts present in experimental images acquired at the European Synchrotron Radiation Facility (ESRF, Grenoble, France). Finally, we investigated the use of different registration methods, one based on cross-correlation and one based on mutual information, for the alignment of Fresnel diffraction patterns acquired at different distances. Applied to experimental data, the mutual information based method was found to be more robust to the type of artefacts encountered in practice.

2 Materials and methods

2.1 Image formation

The experimental set-up of free-space propagation-based tomography is described in Fig. 1. The data simulation is based on the assumption that an object can be fully described by its complex refractive index distribution

$$n(x,y,z) = 1 - \delta_n(x,y,z) + i\beta(x,y,z) \tag{1}$$

where β is the attenuation index and δ_n is the refractive index decrement, which is related to the phase shift that is induced on the incident wave front $u_{inc}(\mathbf{x})$ with $\mathbf{x} = (x,y)$. For X-rays, the real part of n is very close to, but always smaller than, 1 and is therefore usually written as $1 - \delta_n$. Here, z describes the propagation direction and $\mathbf{x} = (x,y)$ are the coordinates of the plane perpendicular to the propagation direction.

At each projection angle θ and distance D, the intensity $I_{\theta,D}(\mathbf{x})$ is measured. It denotes the intensity of the wave $u_{\theta,D}(\mathbf{x})$ after interaction with the object, which is known as an *in-line phase contrast image* or *Fresnel diffraction pattern*. This can be written as

$$I_{\theta,D}(\mathbf{x}) = \left|u_{\theta,D}(\mathbf{x})\right|^2. \tag{2}$$

The wave front $u_{\theta,0}(\mathbf{x})$ at propagation distance zero, i.e. at the exit plane of the object, can be modelled by the multiplication of the incident wave front $u_{inc}(\mathbf{x})$ with the transmittance function of the object

$$T_\theta(\mathbf{x}) = \exp[-B_\theta(\mathbf{x}) + i\varphi_\theta(\mathbf{x})] \tag{3}$$

so that

$$u_{\theta,0}(\mathbf{x}) = T_\theta(\mathbf{x}) u_{inc}(\mathbf{x}) \tag{4}$$

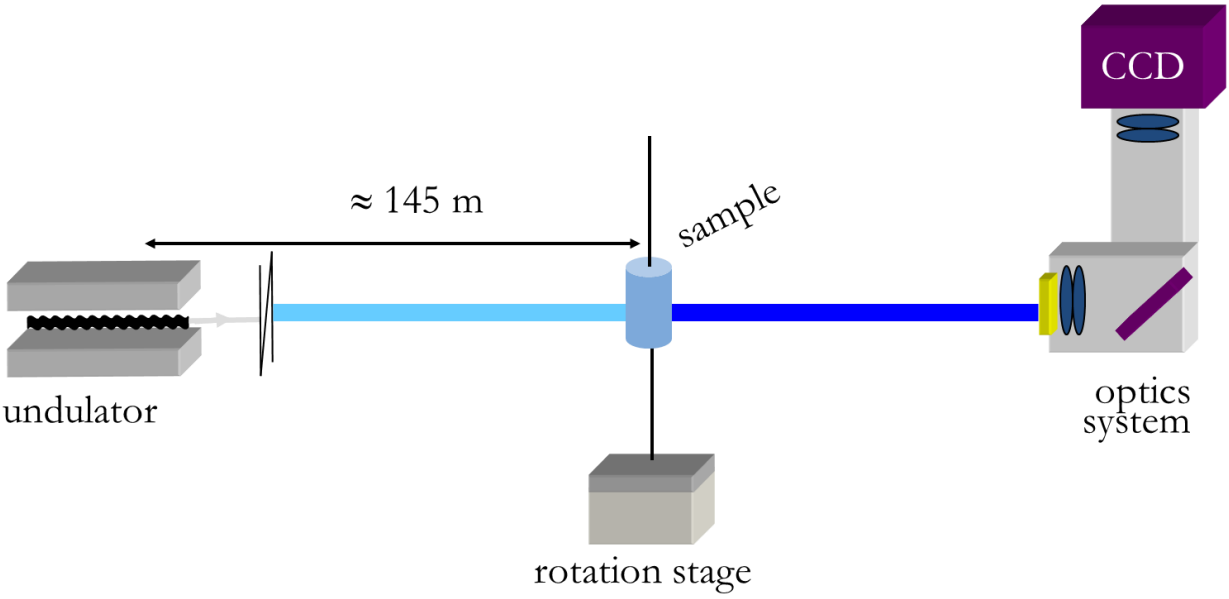

Figure 1: A typical synchrotron radiation X-ray propagation based phase contrast imaging set-up. The sample is mounted on a translation-rotation stage, either directly in the insertion device beam, or in the beam exiting the monochromator optics. The image is recorded on an indirect detection CCD detector.

Usually a flat illumination is assumed, for simplicity, in which case $u_{inc}(\mathbf{x})$ can be dropped. The attenuation $B(\mathbf{x})$ and the phase shift $\varphi(\mathbf{x})$ are projections through the absorption and refractive index distributions

$$B(\mathbf{x}) = \frac{2\pi}{\lambda} \int \beta(\mathbf{x}, z)\, \mathrm{d}z \tag{5}$$

$$\varphi(\mathbf{x}) = -\frac{2\pi}{\lambda} \int \delta_n(\mathbf{x}, z)\, \mathrm{d}z. \tag{6}$$

Propagation over a relatively small distance D can be modelled as a linear system, that is as a convolution with the Fresnel propagator. For our purposes, it is more convenient to express this convolution as a multiplication in the Fourier domain

$$\tilde{u}_D(\mathbf{f}) = \tilde{P}_D(\mathbf{f})\tilde{u}_0(\mathbf{f}) \tag{7}$$

where tilde denotes the Fourier transform and $\mathbf{f} = (f_x, f_y)$ are the frequency coordinates conjugate to $\mathbf{x}$. The Fourier transform of the Fresnel propagator is given by (Goodman, 2005)

$$\tilde{P}_D(\mathbf{f}) = \exp(-i\pi\lambda D|\mathbf{f}|^2) \tag{8}$$

2.2 Simulations

Synthetic projection data were generated by simulating the straight line projections in Eq.(5) and (6) separately, then assembling the resulting wavefield (Eq. 3). Propagation was simulated by implementing Eq. (7), by first taking the FFT of the wavefield, multiplying with Eq.(8), then taking the inverse FFT. The Fresnel diffraction patterns were then obtained by taking the squared modulus of the propagated wave (Eq. 2). To avoid aliasing effects, projections and propagation were simulated on a 2048×2048 grid. The diffraction patterns were then binned to 512×512, to emulate the effect of a CCD detector. Simulated data was generated using a sphere and a modified 3D Shepp-Logan phantom (Langer et al., 2008) at four different propagation distances, assuming fully coherent X-rays of wavelength $\lambda = 0.5166$ Å, corresponding to an X-ray energy of 24 keV. 712 projection angles were used. Projection data was simulated in a parallel geometry, using RTK (Rit et al., 2014) and analytical definitions of the phantoms and calculation of the projections. Propagation and detection was simulated using GNU Octave.

2.2.1 Motion

Different kinds of motion of the sample that could occur during data acquisition were simulated, with the purpose to show their effect on the retrieved phase maps and reconstructed volumes. Therefore, we implemented the following misalignments:

- a constant shift of all projections in each propagation distance, caused for example by a misalignment of the detector when going from one propagation distance to the next,
- a continuous linear shift of the projections, i.e. a drift of the sample or detector during the measurement,
- a random, normally distributed shift of the projections, introduced to model vibration of the equipment during data acquisition.

All shifts are to be understood as shifts of the propagated projections in the projection plane, that is along the x or y axis which were introduced in section 2.1, where the y axis physically is the vertical direction and is parallel to the sample axis of rotation. The magnitude and orientation (horizontal, vertical or both) of the chosen motion type was set separately for each propagation distance.

2.3 Experimental data

The registration algorithms were evaluated on two different experimental data sets: a constructed wire phantom test object using μCT, and a bone micro-pillar sample imaged using phase nano-tomography.

2.3.1 Wire phantom phase *μ*CT

A phantom object was constructed for verification purposes. This phantom is composed of a 99.99 % Al wire (⌀ 125 μm), a bundle of alumina (Al_2O_3) fibers (⌀ 20 μm), polyethylene terephthalate (PET) monofilaments (⌀ 200 μm), and polypropylene (PP) fibers (⌀ 28 μm), fitted inside a Pyrex capillary with 1 mm inner diameter. All materials were acquired from Goodfellow. The phantom was imaged at the ESRF ID19 beamline at 0.7 μm pixel size with an X-ray energy of 22.5 keV selected by a double Si crystal monochromator. 1500 projections were recorded over a 180° range at four sample-to-detector distances D=[2, 10, 20, 45] mm.

2.3.2 Bone micro-pillar phase nano-tomography

Bone micro-pillar samples were prepared at the Institute for Surgical Technology and Biomechanics (ISTB, Bern, Switzerland).) and the Swiss Federal Laboratories of Material Science and Technology (EMPA, Thun, Switzerland). A micro-pillar was sculpted with a focused ion beam (FIB) at the top of a conical compact sheep bone (Schwiedrzik et al., 2014). Image acquisition was made at ID16A beamline (ESRF, Grenoble). The energy of the beam was set to 33.6 keV. 2000 projections were acquired over a 180° range, with an exposure time of 0.4 s per projection. The effective pixel size was 25 nm.

2.4 Phase Retrieval and tomographic reconstruction

The reconstruction in in-line phase tomography is usually split in two steps. First, the phase is retrieved at each rotation angle. Then, the resulting phase maps are used as input to a tomographic reconstruction algorithm.

Phase retrieval is a non-linear inverse problem, due to the squared modulus of the complex wave function in Eq. (2). This expression can be linearised, however, in order to yield efficient phase retrieval algorithms. One approach that uses linearization is called the Contrast Transfer Function (CTF) (P. Cloetens et al., 1999). The transmittance function (Eq. 3) is linearised by a Taylor expansion, keeping only the first order terms (P. Cloetens et al., 1999; Peter Cloetens et al., 2002):

$$T(\mathbf{x}) \approx 1 - B(\mathbf{x}) + i\varphi(\mathbf{x}). \tag{8}$$

This linearisation with respect to the amplitude and phase modulation assumes an object with weak absorption and a slowly varying phase (Jean Pierre Guigay et al., 2007).

Using a representation of the Fourier Transform of the Fresnel diffraction pattern (J.-P. Guigay, 1977)

$$\tilde{I}_D(\mathbf{f}) = \int T\left(\mathbf{x} - \frac{\lambda D\mathbf{f}}{2}\right) T^*\left(\mathbf{x} + \frac{\lambda D\mathbf{f}}{2}\right) \exp(-i2\pi\mathbf{x}\cdot\mathbf{f})\, \mathrm{d}\mathbf{x} \tag{9}$$

and substituting Eq. 8 we have

$$\tilde{I}_D(\mathbf{f}) = \delta_{Dirac}(\mathbf{f}) - 2\cos(\pi\lambda D|\mathbf{f}|^2)\,\tilde{B}(\mathbf{f}) + 2\sin(\pi\lambda D|\mathbf{f}|^2)\tilde{\varphi}(\mathbf{f}) \tag{10}$$

which can be solved for the Fourier transform $\tilde{\varphi}(\mathbf{f})$ of the phase (P. Cloetens et al., 1999). However, the phase factor in Eq. 10 can have zero-crossings, therefore several propagation distances need to be combined in order to cover the whole frequency domain (Zabler et al., 2005). In addition, the factor $\sin(\pi\lambda D|\mathbf{f}|^2)$ also approaches zero for low frequencies which can cause low frequency noise in reconstructions (Max Langer et al., 2008).

For the simulated data we used the CTF model, a linear least squares approach and Tikhonov regularization to retrieve the phase from several distances. For the wire phantom, the mixed approach with a homogeneous object prior was used. For the bone micro pillar, a multi-distance version of Paganin's method (Paganin et al., 2002; Villanova et al., 2014; Yu et al., submitted) using least-squares, followed ba 10-iteration of a non-linear conjugate gradient algorithm. In all cases, filtered backprojection was used to reconstruct the refractive index decrement distriyubution of the sample from the retrieved phase maps. We used the PyHST2 hybrid distributed code for high speed tomographic reconstruction (Mirone et al., 2013).

2.5 Registration of phase contrast images

2.5.1 General scheme

The first aim of the simulations was to show the resulting artefacts due to misalignments of the phase contrast images on the retrieved phase maps and tomographic reconstructions. This can be used by the practitioner to determine if an artefact is due to misalignment. In practice however, when imaging real samples, one wants rather to correct any motion of the sample or detector before carrying out the phase retrieval in order to eliminate as many artefacts from motion as possible. Therefore, several steps for motion correction are carried out before retrieving the phase. The first step consists in a first correction of drift of the sample during the data acquisition. For this purpose, an additional image at a number of projections at specific angles, for example 180°, 90°, and 0° in the case of a 180° degree scan, is recorded once the tomographic scan is completed. These images are then registered to the projections measured during the scan. The resulting measurements are fitted with a sinusoid, which allows correcting for linear displacements of the sample during the scan. The propagation distance that had the least movement is chosen as the target distance to which the other distances will be registered, and the motion correction is applied to this distance. The second step is registration of the phase contrast images at different propagation distances. For every projection at a certain interval, usually every 100 projections, the vertical and horizontal shifts between two successive projection planes are determined. The shifts for all projection angles are calculated by polynomial interpolation using by default a 6^{th} and 2^{nd} order polynomial in the horizontal and vertical direction respectively. This assumes that any motion is smooth, for example due to continuous a drift of the sample.

2.5.2 Cross-correlation based method

Usually, the registration method to determine the shifts was a local search for an optimum of the cross-correlation between the fixed and the moving image. The moving image is translated by shifts that are defined by a given window, usually 5×5. Then, for each shift, the distance measure to the fixed image is evaluated. This method assumes that the shifts between two successive planes are small, since large shifts take longer time to calculate. It is also sensitive to local minima. As an example, Fig. 2 depicts the shift values for 3 propagation planes with respect to a so-called "reference plane" that is kept stationary. The vertical displacement is reported on the left, and the horizontal on the right. The blue line corresponds to measured shift values, in this case every 100 projections. The red curve is the corresponding polynomial fit.

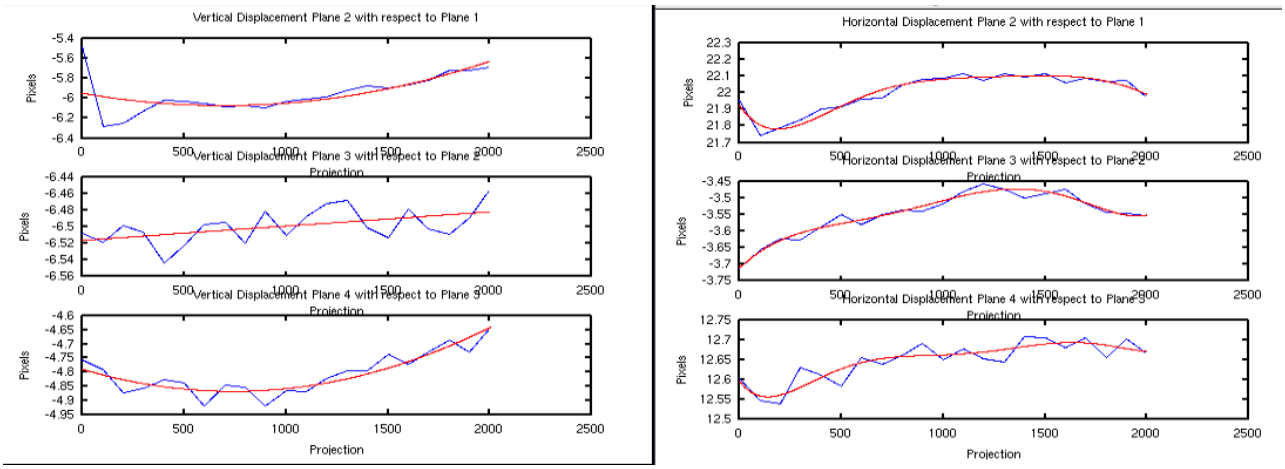

Figure 2: Example of shifts curves. The projection number is reported on the abscissa, and the shift value (in pixels) on the ordinate. The blue line is drawn from a measurements every 100 projections and the red curve corresponds to the polynomial fit. Note that the difference between measured and fitted values is less than one pixel in all plots, which is characteristic for a successful registration, and a stable scan.

2.5.3 Mutual Information method

As an alternative to the cross-correlation based method, we evaluated a mutual information (MI) based registration algorithm. MI is usually employed in multi-modality imaging, where the contrast can be different in the two images (Maes et al., 1997; Viola & Wells, 1997). It has the major advantage to be invariant to intensity changes between images, for example inversion contrast. Consider two images A and B. Their pixels are indexed by a and b, respectively. The MI index of A and B is expressed as

$$MI(A,B) = \sum_{a\in A}\sum_{b\in B} p_{AB}(a,b)\log\left(\frac{p_{AB}(a,b)}{p_A(a)p_B(b)}\right) \tag{11}$$

where $p_{AB}(a,b)$ is the joint probability distribution function of A and B, $p_A(a)$ and $p_B(b)$ the marginal probability distribution functions of A and B, respectively.

The MI index of two images can be zero or positive; it is equal to 0 if the two images are independent, and increases with the similarity of the two images. In our case, we can have substantially different contrast in the images to be registered, due to strong interference fringes that change as propagation distance changes. The idea behind this method is to assume a mapping between the intensities of the two images without assuming a specific functional mapping (identity, linearity, etc).

We implemented this approach by interfacing *Elastix* (Klein et al., 2010; Shamonin et al., 2013) from GNU Octave. The choice of *Elastix* was based on features such as a variety of different similarity measures, and multi-resolution optimisation strategies, which could useful in the case of larger shifts. Since the computation time needed for the registration of each projection angle increases when using more advanced similarity measures, it is advisable to perform the computations in parallel. We also included the possibility to take into account rotation and magnification in the image transformations. This allows to correct, for example, for roll in the translation stage, and imprecision or drift of the z position of the sample. The latter can be useful if the computed theoretical value of magnification does not accord with the actual magnification of the projections in the case of cone beam tomography.

2.6 Quantification of resolution

The loss of resolution in the reconstructed image due to the misalignments was evaluated for random normally distributed shifts with different standard deviations σ. For this purpose, edge profiles of the boundary of the reconstructed sphere phantom were calculated at several positions, always perpendicular to the boundary. In the theoretical case of perfect reconstruction of the underlying phantom volume, the line profiles should be step functions. Thus one can interpret the measured edge profile as the edge spread function (ESF) of the imaging system. From the ESF, one can then calculate the line spread function (LSF) by taking the derivative of the ESF (Ahmed, 2015). Here, this was done analytically by fitting the ESF with a sum of error functions, which yields a sum of Gaussians as derivative. The LSF can then be used to determine the system's resolution. We chose the full width at half maximum (FWHM) of the LSF as a measure of the resolution.

The goodness of fit of the ESF was evaluated by calculating the coefficient of determination

$$R^2 = 1 - \frac{\sum_{j=1}^{N}(r_j - \hat{r}_j)^2}{\sum_{j=1}^{N}(r_j - \bar{r}_j)^2}$$

where N is the number of measured points, r_j is the jth measured point, $\hat{r}_j$ is the corresponding point of the fitted function and $\bar{r}_j$ is the mean of the measured data points.

3 Results

3.1 Simulations

3.1.1 Detector misalignment

We simulated a horizontal shift of 5 pixels of the projections in the longest propagation distance. The remaining propagation distances were left aligned. Fig. 3 (a) and (b) shows the resulting phase maps that were retrieved by using the phase retrieval method described in section 2.3.1 for the sphere and the modified 3D Shepp-Logan phantom, respectively. For both phantoms we can observe a doubling of structures or a ghost image in the direction where the shift was applied. Further, both phase maps are subject to low frequency noise. This indicates that poor alignment of phase contrast images could contribute to low frequency noise in the retrieved phase. The regularization parameter in the phase retrieval was chosen to minimize this noise by visual evaluation. In Fig. 3 (c) and (d) the corresponding phase tomograms are shown. Also here a characteristic doubling of features, or ghost image, can be seen. It can be noted that this artefact is similar to the one arising from a poorly adjusted rotation axis in standard tomography. It could therefore be confounded with this error source in practice.

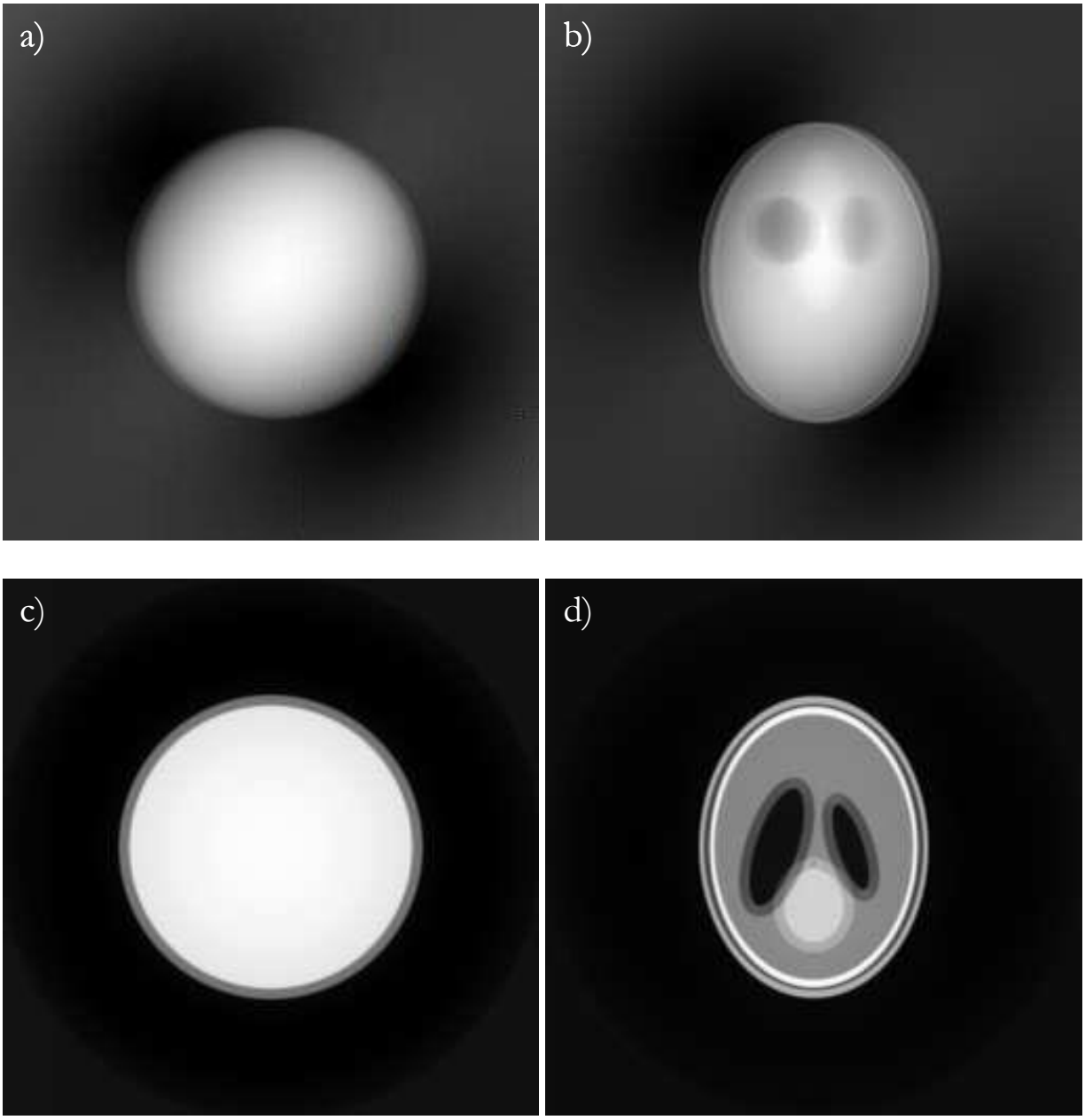

Figure 3: Phase maps and phase tomograms of two phantoms retrieved from simulated diffraction patterns with a constant shift of 5 pixels in the longest propagation distance. (a) Sphere phantom, (b) modified 3D Shepp-Logan phantom. Note the characteristic doubling of image features, or ghost image, in both images. Note also the presence of low-frequency noise. (c) Reconstructed phase tomographic slice of the sphere and (d) the 3D Shepp-Logan phantom. Also in the object domain we can observe a characteristic doubling of features or ghost image.

3.1.2 Sample drift

To investigate the effect of linear drift of the sample during the data acquisition, a continuously increasing shift was applied to the projections of the longest propagation distance. The maximum shift was reached in the last projection angle, at a little bit less than 360º. The projections in the remaining distances were left unchanged. Fig. 4 shows the resulting tomographic reconstruction for a horizontal drift with a maximal shift of 5 pixels. In the reconstruction the drift results in blur and a characteristic spiral shaped artefact.

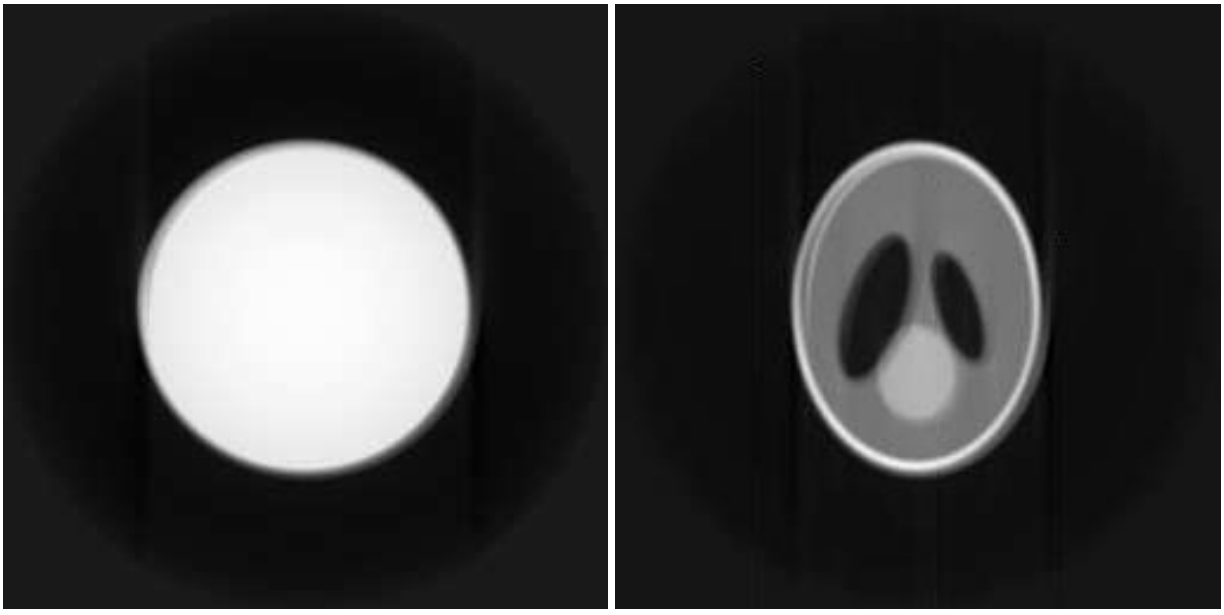

Figure 4: Reconstructed slices of two different phantoms where a linear drift with a maximal shift of 5 pixels at the last projection angle was applied in the longest propagation distance.

3.1.3 Vibration

Normally distributed horizontal and vertical shifts with zero mean and a range of different standard deviations were applied on all projections in all propagation distances to model vibration during the data acquisition. Fig. 5 shows the reconstruction with application of random shifts with a standard deviation of one pixel. For comparison, the reconstruction when no motion is applied is also shown. As one might expect, the random shift leads to a blurring of the object.

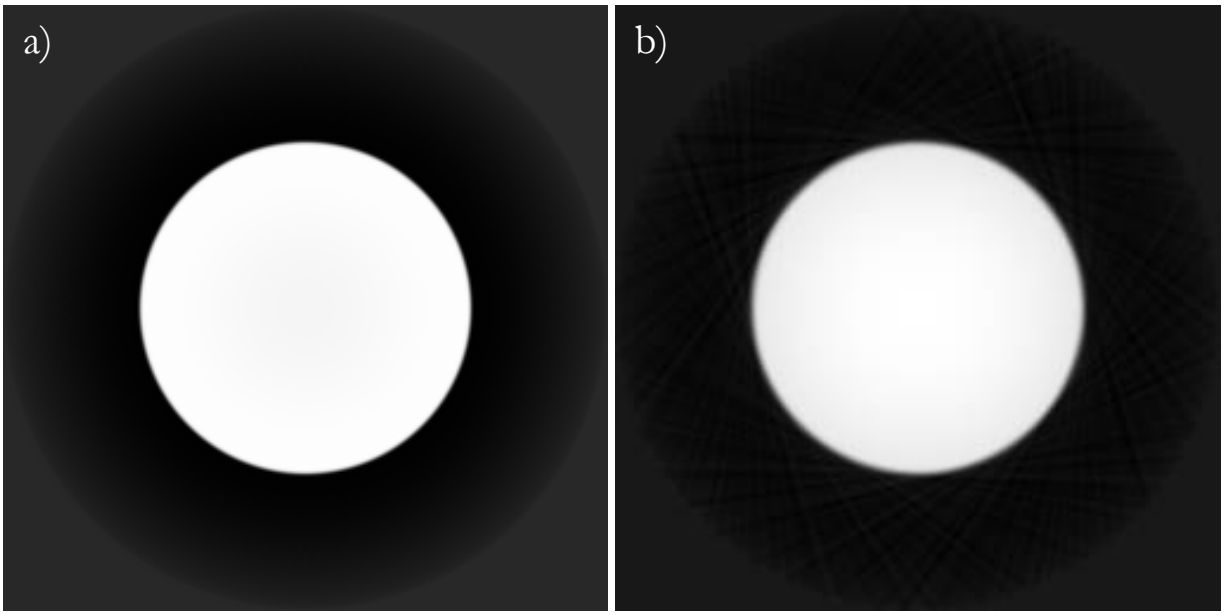

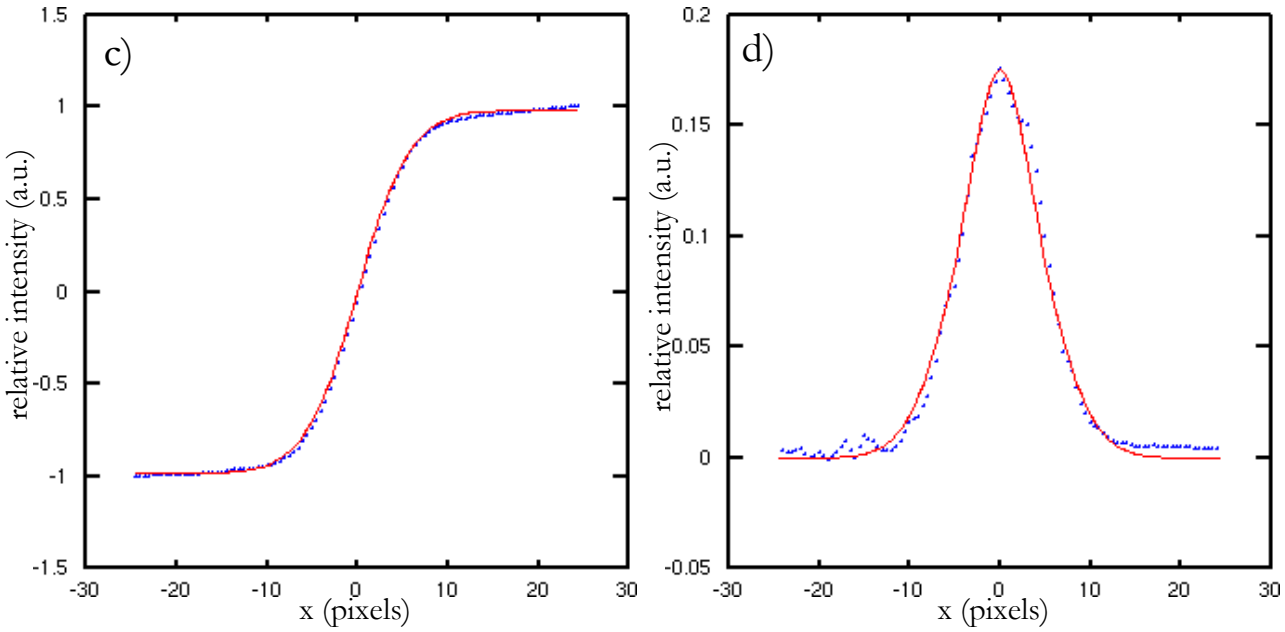

Figure 5: Reconstruction from phase maps retrieved from (a) non-shifted diffraction patterns, (b) randomly shifted diffraction patterns with a standard deviation of one pixel. (c) ESF and (d) LSF for a random motion with standard deviation σ=4. (c) Measured ESF (blue dots) and fit with a sum of error functions (red line). (d) LSF calculated numerically (blue dots) and analytically from fit (red line).

The loss in resolution in the reconstruction was evaluated for different standard deviations σ of the random shifts as described in Section 2.2.1. Fig. 5 (c) shows the edge spread function and a fit for shifts with a standard deviation of σ=4, as well as the numerical and analytical derivative (Fig. 5 (d)), that is the line spread function. For each of the different standard deviations ranging between zero and five, the coefficient of determination was $R^2 > 0.99$. Fig. 5 (a) shows a plot of the calculated FWHM of the LSF against the standard deviation. A linear fit was calculated with a coefficient of determination $R^2 = 0.98$ and a slope of m=4.38.

For comparison, the calculation of the FWHM of the LSF was also carried out in the case of attenuation-based CT. In this case, random shifts were applied to the non-propagated projections which were then reconstructed. Surprisingly, the FWHM in the case of phase tomography and attenuation based CT are very similar.

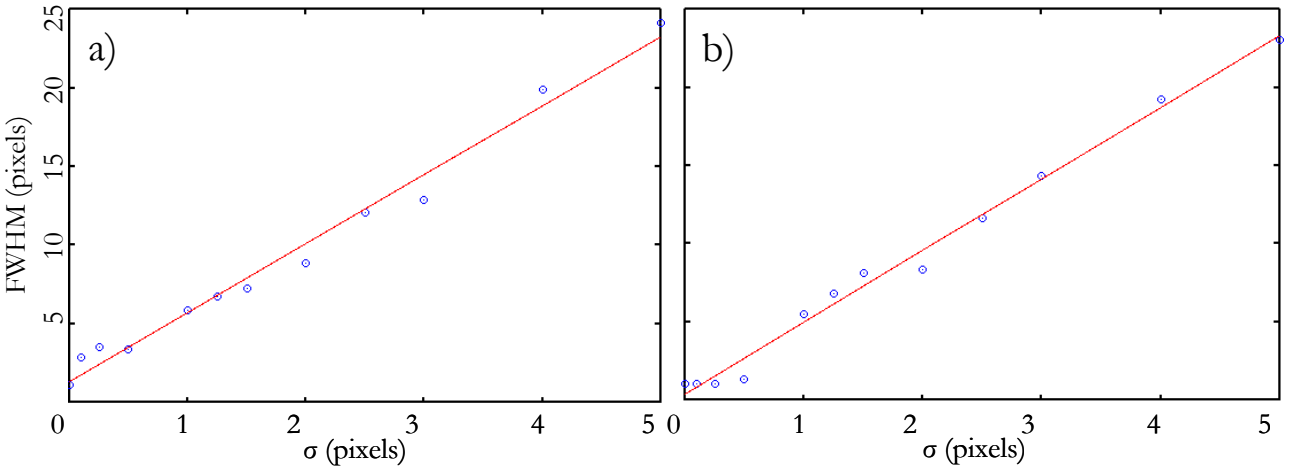

Figure 6: Full width at half maximum (FWHM) of the line spread function plotted against the standard deviation of the random shifts together with a linear least squares fit of the obtained points for (a) phase tomography and (b) attenuation-based CT. Goodness of fit: (a) $R^2 = 0.98$ (b) $R^2 = 0.99$. Slope of regression line: (a) m=4.38 (b) m=4.59.

3.1.4 Comparison with experimental data

Projection data of the phantom in Section 2.1.1 was reconstructed, a slice is shown in figure Fig. 7. Correction for motion including sample drift and registration of corresponding projections at different propagation distances was performed using the correlation-based approach as described in Section 2.4. The phase was retrieved using the mixed approach with a homogeneous object prior (Guigay et al. 2007; Langer et al., 2010). The regularization parameter in the phase retrieval was chosen with the L-curve criterion.

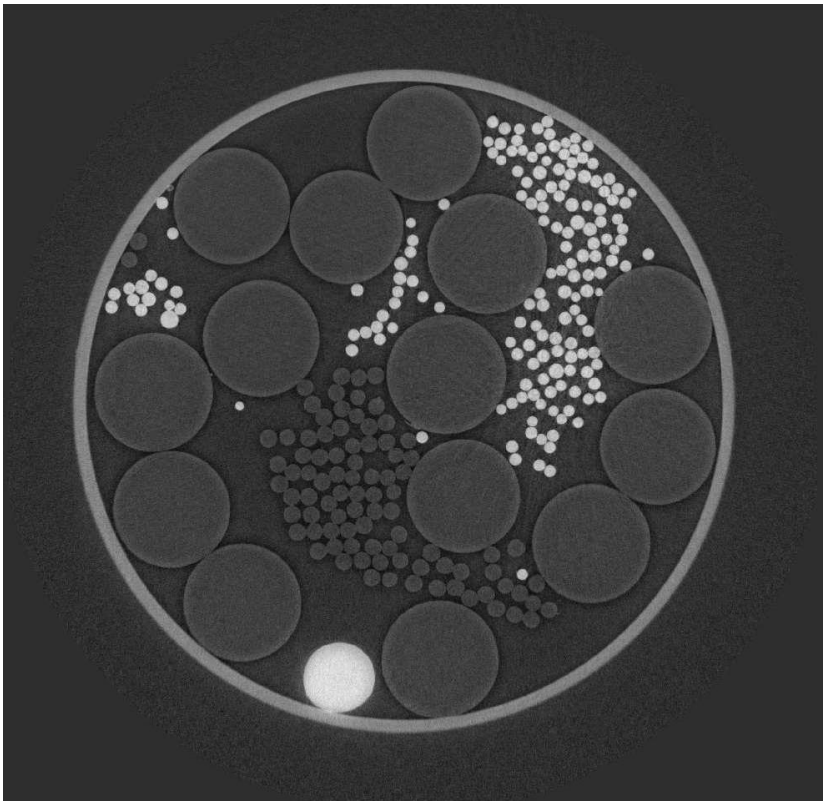

Figure 7: Reconstructed slice of a phantom object acquired at the ESRF ID19 beamline. Correction for sample drift and registration of projections using cross-correlation were performed

For comparison with the artefacts found in our simulations, we repeated the reconstruction of the phantom several times, omitting different steps in the motion correction procedure to emulate a failed registration. A detail of the resulting reconstructions is shown in Fig. 8, where (a) corresponds to the reconstruction from Fig. 7. First, we omitted the registration but corrected for sample drift, and the distances were roughly aligned by registering the projections of the first projection angle only and applying the same shift to all projection angles (Fig. 8 (b)). Then, we omitted the registration as well as the rough alignment of the planes, the reconstruction is shown in Fig. 8 (c). Last, we also omitted the sample drift correction, performing no motion correction at all. Some of the arising artefacts are indicated by arrows. The artefacts we observed for constant shifts (Fig. 2) are visible in Fig. 8 (b) and (c). Both constant shift and motor drift artefacts are visible in Fig. 8 (d). Comparing the different subfigures we see that most of the artefacts arise when we do not perform the rough alignment of the different projection planes. This suggests that the principal motion in this particular measurement might be due to a slightly misaligned detector translation stage. In contrast to the rough alignment, the registration of every 100th projection does not have a visible impact on the reconstruction quality, which suggests remaining motion after motion correction is small in this case.

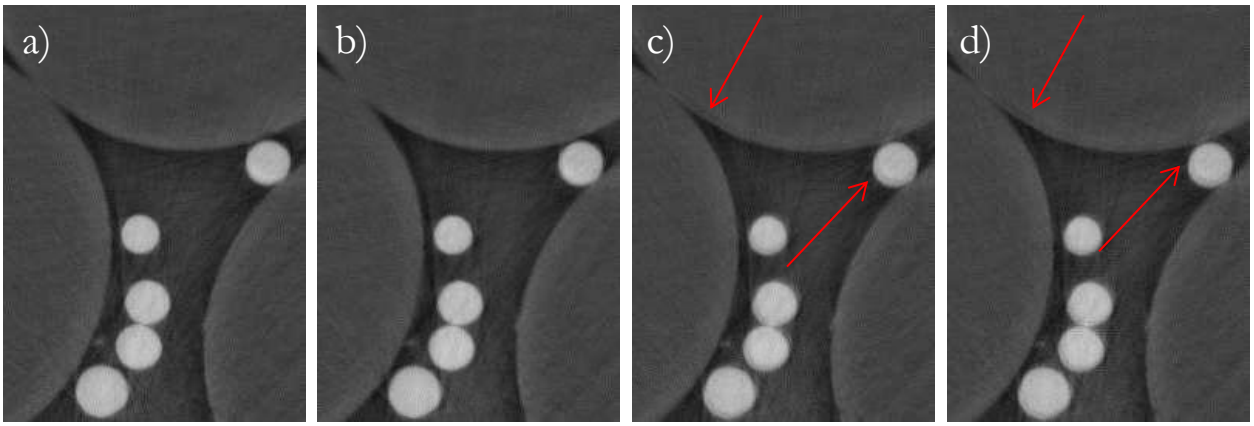

Figure 8: Reconstruction of projection data acquired at the European Synchrotron Radiation Facility, performing different steps in the motion correction procedure. (a) Correction for sample drift and registration of every 100th projection followed by a fit of shifts. (b) Correction for sample drift and rough alignment by registering the first projection only. (c) Correction for sample drift but no rough alignment of the planes, no registration. Artefacts indicated by arrows. (d) No pre-processing for motion correction, neither sample drift nor registration of projections. Artefacts indicated by arrows.

3.2 Mutual information for registration of Fresnel diffraction patterns on experimental data

3.2.1 Wire phantom phase *μ*CT

We applied three registration algorithms on the phantom data in Fig. 7: based on cross-correlation, normalised mutual information, and normalised cross-correlation, respectively. In this data set, the shifts between the projections are quite small, therefore the correlation-based local search that was mentioned in section 2.4 should yield good results and is used as a reference. Fig. 9 shows a detail of the reconstruction for the different registration methods. If we examine the resulting phase maps and tomographic reconstructions, it is not obvious which approach gives the most correct registration and thus the best reconstruction. This is the expected outcome since the shifts are small, the propagation distance was relatively small and no particular optics were used so that the contrast was quite similar between the different distances.

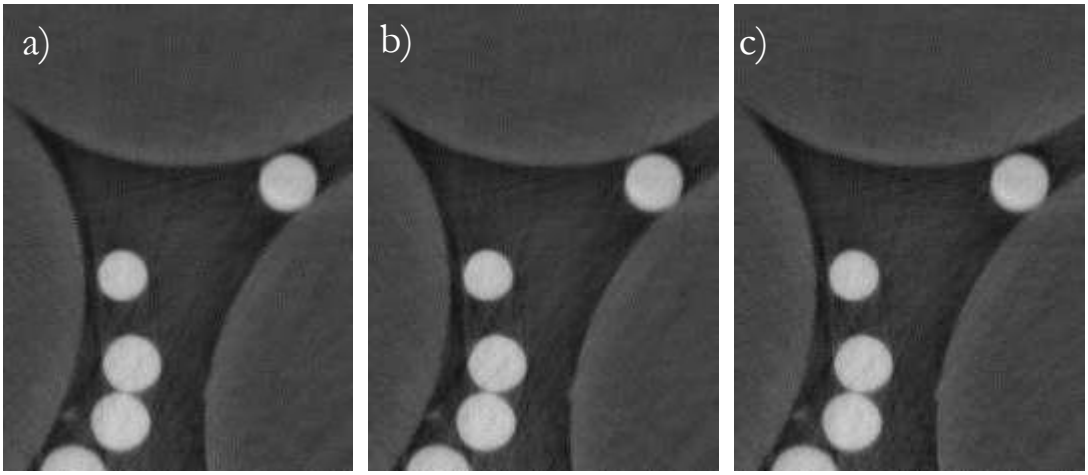

Figure 9: Detail of a reconstruction where the registration step was carried out using different approaches: (a) correlation-based registration, (b) normalized cross correlation, (c) normalized mutual information. Quality of reconstruction is not strongly affected, indicating that the three algorithms yielded acceptable results in this case.

3.2.2 Bone micro-pillar phase nano-tomography

To show the global morphology of the sample, a 3D rendering of the whole scanned volume is shown in **Error! Reference source not found.**. The micro-pillar is seen on top of a larger base.

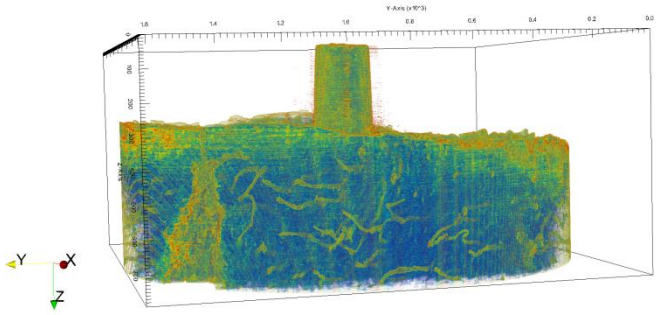

Figure 10: Volume rendering of a micro-pillar sample. The box is 51μm (X) by 51μm (Y) by 19.9μm (Z). A lacuna and canaliculi are visible in the base.

We compared the classical correlation based method and the registration method using MI on this sample. The results are shown in Figure 11, for two different vertical positions in the sample. In this case, the MI based algorithm performs better than the correlation-based one. On the slices reconstructed with the correlation-based approach misalignment artefacts are clearly visible (Fig. 11 (a)), as opposed to the slices reconstructed using the MI based algorithm where image quality is substantially improved (Fig. 11 (b)).

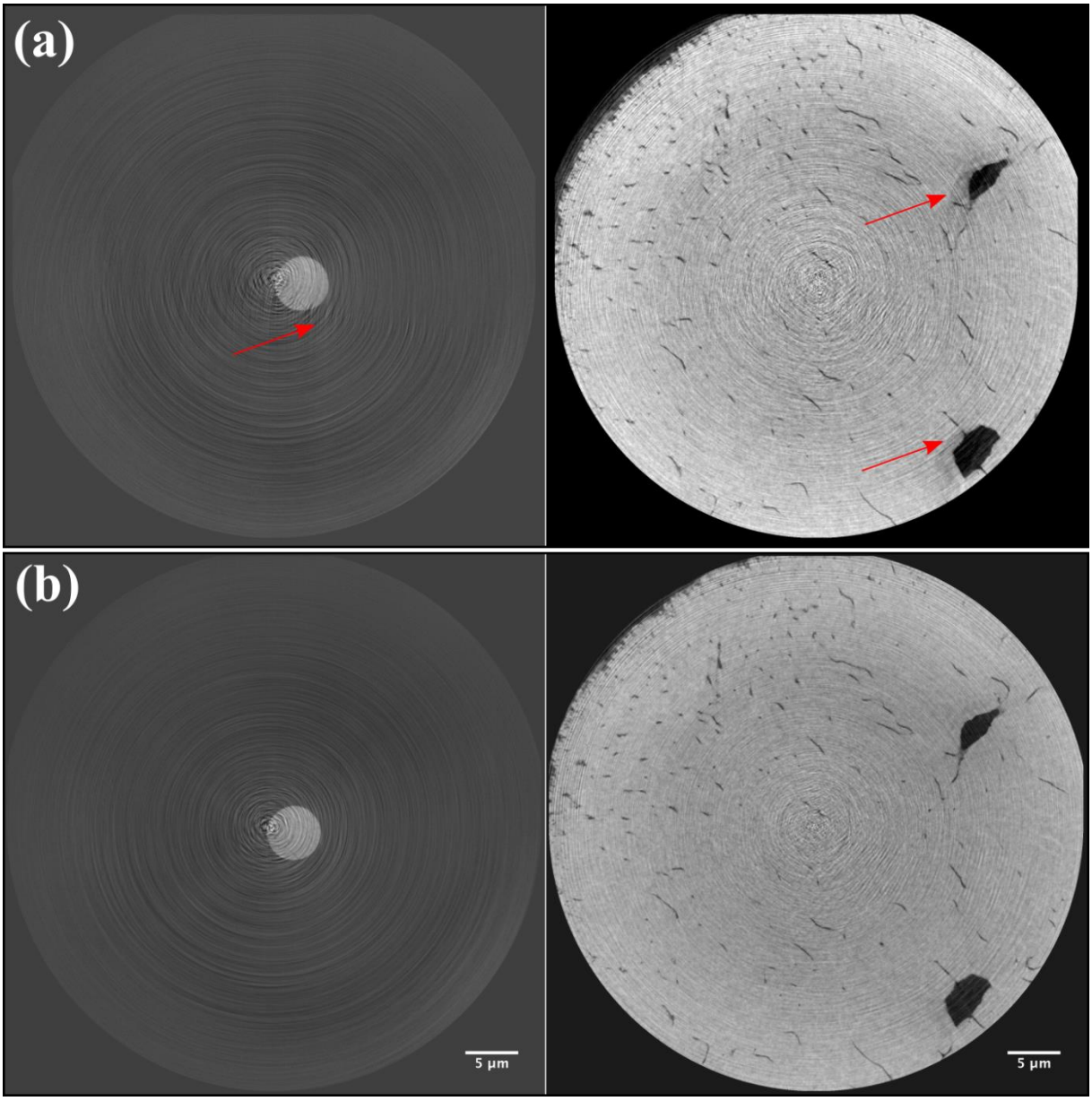

Figure 11: Example of phase δ_n volume after registering the projections using (a) a correlation-based method; (b) the MI-based method. The left column shows a slice in the micro-pillar part, and the right column a slice in the base of the micro-pillar, made of bone. The red arrows highlight typical misalignments artefacts.

4 Discussion and conclusion

We investigated the impact of misalignment of in-line phase contrast images on the resulting phase tomography images. Different kinds of motion during the data acquisition were simulated on synthetic data. We showed that the misalignment of the projections of different propagation distances at a given projection angle results in a particular doubling of structure artefact both in the retrieved phase map and the phase tomogram. The artefact somewhat resembles the artefact observed in attenuation-based CT for a poorly chosen rotation axis and could be confused for this. A linear drift of the sample yielded a characteristic spiral shaped artefact. In the case of vibrations, which were modelled using normally distributed random shifts of the phase contrast images, we observed a blurring of the reconstruction. A sensitivity analysis showed a linear dependence between the system resolution and the standard deviation of the vibration. Moreover, the magnitude of the blur is comparable to the case of vibration in attenuation-based CT. Hence, in-line phase tomography using several distances is not more sensitive to vibrations than attenuation or single-distance phase imaging.

Comparison of the simulated artefacts with real data acquired at the ESRF ID19 beamline on a constructed phantom showed the same types of artefacts mentioned above, and suggests the presence of shifts of the detector (due to a misaligned camera translation stage) and sample drift (due to motor instabilities) in the measurement setup. However, the drift does not necessarily need to be linear as assumed in our simulations. Since the drift and shift were rather small, the improvement in image quality that we achieved by additionally registering the projections of different propagation distances at every 100th projection angle was rather small. Finally, when comparing different registration approaches, based on cross-correlation, normalised cross-correlation and mutual information, the quality of the reconstruction was not greatly improved. This was due to relatively weak defocusing conditions (hence contrast at the different distances remain quite similar), absence of strong periodic artefacts in the phase contrast images, and the relatively small shifts.

Applying the mutual-information based method on nano-tomography data acquired at the ESRF ID16A beamline, however, yielded substantial improvements. This data shows strong periodical artefacts, and the contrast changes substantially between the imaging planes. This causes cross-correlation based methods to fail since the hypothesis of linearly dependent contrast between the images is violated. The periodic artefact also creates a strong local optimum in the cross-correlation. The images could be registered using the mutual information based approach, however. This is probably due to no underlying hypothesis on the contrast in the images (mutual information is actually often used in registration of images from different imaging modalities), as well as a lower sensitivity to periodic structures.

In conclusion, registration of phase contrast images seems to be a crucial step in obtaining high quality reconstructions of the phase and consequently the refractive index decrement. This problem is scarcely mentioned in literature, however. We showed that selection of a registration algorithm that fits the characteristic of the phase contrast images is necessary for the registration to be robust to the changing contrast and the types of image artefacts encountered. These results should improve the rate of successful reconstructions in in-line phase nano-tomography, and reduce operator time for manual registration when correlation-based registration algorithms fail.

5 Acknowledgements

We acknowledge the ESRF for the allocation of beamtime thought the Long Term Project (LTP) MD830. We further acknowledge Pr. Philippe Zysset (University of Bern, Switzerland) for the micro-pillar preparation and transport. This work was performed within the framework of the LABEX PRIMES (ANR-11-LABX-0063), Université de Lyon, part of the Investissements d'Avenir programme (ANR-11-IDEX-0007), operated by the French National Research Agency (ANR).

6 References

Ahmed, S. N. (2015). *Physics and Engineering of Radiation Detection*. *Physics and Engineering of Radiation Detection*. http://doi.org/10.1016/B978-0-12-801363-2.00001-2

Boistel, R., Aubin, T., Cloetens, P., Langer, M., Gillet, B., Josset, P., … Herrel, A. (2011). Whispering to the deaf: communication by a frog without external vocal sac or tympanum in noisy environments. *Plos one*, *6*(7), e22080.

Cloetens, P., Ludwig, W., Baruchel, J., Van Dyck, D., Van Landuyt, J., Guigay, J. P., & Schlenker, M. (1999). Holotomography: Quantitative phase tomography with micrometer resolution using hard synchrotron radiation x rays. *Applied Physics Letters*, *75*(19), 2912. http://doi.org/10.1063/1.125225

Cloetens, P., Ludwig, W., Boller, E., Peyrin, F., Chlenker, M., & Baruchel, J. (2002). 3D imaging using coherent synchrotron radiation. *Image Analysis & Stereology*, *21*(4), S75–S85. http://doi.org/10.5566/ias.v21.pS75-S85

Cloetens, P., Pateyron-Salomé, M., Buffière, J. Y., Peix, G., Baruchel, J., Peyrin, F., & Schlenker, M. (1997). Observation of microstructure and damage in materials by phase sensitive radiography and tomography. *Journal of Applied Physics*, *81*(9), 5878. http://doi.org/10.1063/1.364374

Frachon, T., Weber, L., Hesse, B., Rit, S., Dong, P., Olivier, C., … Langer, M. (2015). Dose fractionation in synchrotron radiation x-ray phase micro-tomography. *Physics in Medicine and Biology*, *60*(19), 7543–7566. http://doi.org/10.1088/0031-9155/60/19/7543

Goodman, J. W. (2005). *Introduction to Fourier Optics,* 3rd edition, Englewood, CO: Roberts.

Guigay, J.-P. (1977). Fourier transform analysis of fresnel diffraction patterns and in-line holograms. *Optik*, *49*, 121–125.

Guigay, J. P., Langer, M., Boistel, R., & Cloetens, P. (2007). Mixed contrast transfer and transport of intensity approach for phase retrieval in the Fresnel region. *Optics Letters*, *32*, 1617{\textendash}1619. http://doi.org/10.1364/OL.32.001617

Guigay, J. P., Langer, M., Boistel, R., & Cloetens, P. (2007). Mixed transfer function and transport of intensity approach for phase retrieval in the Fresnel region. *Optics Letters*, *32*(12), 1617–1619. http://doi.org/10.1364/OL.32.001617

Herman, G. T. (2009). *Fundamentals of Computerized Tomography*. London: Springer London. http://doi.org/10.1007/978-1-84628-723-7

Horng, A., Brun, E., Mittone, A., Gasilov, S., Weber, L., Geith, T., … Coan, P. (2014). Cartilage and soft tissue imaging using X-rays: propagation-based phase-contrast computed tomography of the human knee in comparison with clinical imaging techniques and histology. *Investigative Radiology*, *49*(9), 627–34. http://doi.org/10.1097/RLI.0000000000000063

Klein, S., Staring, M., Murphy, K., Viergever, M. A., & Pluim, J. P. W. (2010). elastix: a toolbox for intensity-based medical image registration. *IEEE Transactions on Medical Imaging*, *29*(1), 196–205. http://doi.org/10.1109/TMI.2009.2035616

Langer, M., Cloetens, P., Guigay, J.-P., & Peyrin, F. (2008). Quantitative comparison of direct phase retrieval algorithms in in-line phase tomography. *Medical Physics*, *35*(10), 4556–4566. http://doi.org/10.1118/1.2975224

Langer, M., Cloetens, P., Hesse, B., Suhonen, H., Pacureanu, A., Raum, K., & Peyrin, F. (2014). Priors for X-ray in-line phase tomography of heterogeneous objects. *Philosophical Transactions of the Royal Society A*, *372*, 20130129.

Langer, M., Cloetens, P., Pacureanu, A., & Peyrin, F. (2012). X-ray in-line phase tomography of multimaterial objects. *Optics Letters*. http://doi.org/10.1364/OL.37.002151

Langer, M., Cloetens, P., & Peyrin, F. (2010). Regularization of phase retrieval with phase-attenuation duality prior for 3-D holotomography. *IEEE Transactions on Image Processing*, *19*(9), 2428–2436.

Langer, M., Hesse, B., Pacureanu, A., Suhonen, H., Cloetens, P., Raum, K., & Peyrin, F. (2013). Priors for X-ray in-line phase tomography of heterogeneous objects. In *Philosophical Transactions of the Royal Society A,* 372, p. 20130129.

Langer, M., Pacureanu, A., Suhonen, H., Grimal, Q., Cloetens, P., & Peyrin, F. (2012). X-ray phase nanotomography resolves the 3D human bone ultrastructure. *Plos one*, *7*(8), e35691. http://doi.org/10.1371/journal.pone.0035691

Maes, F., Collignon, A., Vandermeulen, D., Marchal, G., & Suetens, P. (1997). Multimodality image registration by maximization of mutual information. *IEEE Transactions on Medical Imaging*, *16*(2), 187–198. http://doi.org/10.1109/42.563664

Mirone, A., Gouillart, E., Brun, E., Tafforeau, P., & Kieffer, J. (2013). PyHST2: an hybrid distributed code for high speed tomographic reconstruction with iterative reconstruction and a priori knowledge capabilities. *NIMA B, 324*, pp. 41-48.

Momose, A., & Fukuda, J. (1995). Phase-contrast radiographs of nonstained rat cerebellar specimen. *Medical Physics*, *22*(4), 375–9. Retrieved from http://www.ncbi.nlm.nih.gov/pubmed/7609717

Nugent, K., Gureyev, T., Cookson, D. D., Paganin, D., & Barnea, Z. (1996). Quantitative Phase Imaging Using Hard X Rays. *Physical Review Letters*, *77*, 2961–2964. http://doi.org/10.1103/PhysRevLett.77.2961

Op de Beeck, M., Van Dyck, D., & Coene, W. (1996). Wave function reconstruction in HRTEM: the parabola method. *Ultramicroscopy*, *64*(1–4), 167–183. http://doi.org/10.1016/0304-3991(96)00058-7

Paganin, D., Mayo, S. C., Gureyev, T. E., Miller, P. R., & Wilkins, S. W. (2002). Simultaneous phase and amplitude extraction from a single defocused image of a homogeneous object. *Journal of Microscopy*, *206*(1), 33–40. http://doi.org/10.1046/j.1365-2818.2002.01010.x

Rit, S., Vila Oliva, M., Brousmiche, S., Labarbe, R., Sarrut, D., Sharp, G. C., … (2014). The Reconstruction Toolkit (RTK), an open-source cone-beam CT reconstruction toolkit based on the Insight Toolkit (ITK). *Journal of Physics: Conference Series*, *489*(1), 12079. http://doi.org/10.1088/1742-6596/489/1/012079

Schwiedrzik, J., Raghavan, R., Bürki, A., LeNader, V., Wolfram, U., Michler, J., & Zysset, P. (2014). In situ micropillar compression reveals superior strength and ductility but an absence of damage in lamellar bone. *Nature Materials*, *13*(7), 740–747. http://doi.org/10.1038/nmat3959

Shamonin, D. P., Bron, E. E., Lelieveldt, B. P. F., Smits, M., Klein, S., Staring, M., (2013). Fast parallel image registration on CPU and GPU for diagnostic classification of Alzheimer's disease. *Frontiers in Neuroinformatics*, *7*, 50. http://doi.org/10.3389/fninf.2013.00050

Snigirev, A., Snigireva, I., Kohn, V., Kuznetsov, S., & Schelokov, I. (1995). On the possibilities of x-ray phase contrast microimaging by coherent high-energy synchrotron radiation. *Review of Scientific Instruments*, *66*(12), 5486. http://doi.org/10.1063/1.1146073

Teague, M. R. (1982). Irradiance moments: their propagation and use for unique retrieval of phase. *Journal of the Optical Society of America*, *72*(9), 1199. http://doi.org/10.1364/JOSA.72.001199

Villanova, J., Cloetens, P., Suhonen, H., Laurencin, J., Usseglio-Viretta, F., Lay, E., … Martin, C. L. (2014). Multi-scale 3D imaging of absorbing porous materials for solid oxide fuel cells. *Journal of Materials Science*, *49*(16), 5626–5634. http://doi.org/10.1007/s10853-014-8275-3

Viola, P., & Wells III, W. M. (1997). Alignment by Maximization of Mutual Information. *International Journal of Computer Vision*, *24*(2), 137–154. http://doi.org/10.1023/A:1007958904918

Yu, B., Weber, L., Pacureanu, A., Langer, M., Olivier, C., Cloetens, P., & Peyrin, F. (Submitted). Filtering approaches for phase retrieval in magnified phase nano-CT: application to bone tissue. *Medical Physics*.

Zabler, S., Cloetens, P., Guigay, J.-P., Baruchel, J., & Schlenker, M. (2005). Optimization of phase contrast imaging using hard x rays. *Review of Scientific Instruments*, *76*(7), 73705. http://doi.org/10.1063/1.1960797

Zanette, I., Daghfous, G., Weitkamp, T., Gillet, B., Adriaens, D., Langer, M., … Boistel, R. (2013). Looking Inside Marine Organisms with MRI and X-ray Tomography. In E. G. Reynaud (Ed.), *Imaging Marine Life*. Wiley-VCH Verlag GmbH & Co. KGaA, Weinheim, Germany. http://doi.org/10.1002/9783527675418.ch

Zanette, I., Weitkamp, T., Lang, S., Langer, M., Mohr, J., David, C., & Baruchel, J. (2011). Quantitative phase and absorption tomography with an X-ray grating interferometer and synchrotron radiation. *Physica Status Solidi A*.